

AD \_\_\_\_\_

Award Number: DAMD17-97-1-7143

TITLE: 3-D Digital Imaging of Breast Calcifications:  
Improvements in Image Quality, and Development of  
Automated Reconstruction Methods

PRINCIPAL INVESTIGATOR: Andrew D. Maidment, Ph.D.

CONTRACTING ORGANIZATION: Thomas Jefferson University  
Philadelphia, Pennsylvania 19107

REPORT DATE: September 2002

TYPE OF REPORT: Final

PREPARED FOR: U.S. Army Medical Research and Materiel Command  
Fort Detrick, Maryland 21702-5012

DISTRIBUTION STATEMENT: Approved for Public Release;  
Distribution Unlimited

The views, opinions and/or findings contained in this report are those of the author(s) and should not be construed as an official Department of the Army position, policy or decision unless so designated by other documentation.

20030513 095

# REPORT DOCUMENTATION PAGE

Form Approved  
OMB No. 074-0188

Public reporting burden for this collection of information is estimated to average 1 hour per response, including the time for reviewing instructions, searching existing data sources, gathering and maintaining the data needed, and completing and reviewing this collection of information. Send comments regarding this burden estimate or any other aspect of this collection of information, including suggestions for reducing this burden to Washington Headquarters Services, Directorate for Information Operations and Reports, 1215 Jefferson Davis Highway, Suite 1204, Arlington, VA 22202-4302, and to the Office of Management and Budget, Paperwork Reduction Project (0704-0188), Washington, DC 20503

1. AGENCY USE ONLY (Leave blank)

2. REPORT DATE

September 2002

3. REPORT TYPE AND DATES COVERED

Final (15 Aug 97 - 14 Aug 02)

4. TITLE AND SUBTITLE

3-D Digital Imaging of Breast Calcifications:  
Improvements in Image Quality, and Development of  
Automated Reconstruction Methods

5. FUNDING NUMBERS

DAMD17-97-1-7143

6. AUTHOR(S) :

Andrew D. Maidment, Ph.D.

7. PERFORMING ORGANIZATION NAME(S) AND ADDRESS(ES)

Thomas Jefferson University  
Philadelphia, Pennsylvania 19107

E-Mail: Andrew.Maidment@mail.tju.edu

8. PERFORMING ORGANIZATION  
REPORT NUMBER

9. SPONSORING / MONITORING AGENCY NAME(S) AND ADDRESS(ES)

U.S. Army Medical Research and Materiel Command  
Fort Detrick, Maryland 21702-5012

10. SPONSORING / MONITORING  
AGENCY REPORT NUMBER

11. SUPPLEMENTARY NOTES

Original contains color plates: All DTIC reproductions will be in black and white.

12a. DISTRIBUTION / AVAILABILITY STATEMENT

Approved for Public Release; Distribution Unlimited

12b. DISTRIBUTION CODE

13. Abstract (Maximum 200 Words) (abstract should contain no proprietary or confidential information)

In this grant, we generated a manually segmented and paired dataset of 110 patients images, which we have used as a "gold standard" in the evaluation of computer algorithms for identifying, segmenting and correlating calcifications. We have been able to develop two separate computer algorithms, one for identification and segmentation of potential calcifications, the other to find calcification triplets that should be paired. Both algorithms are quite robust. There are a number of significant findings from this work that will be published. First, the use of Euler's number to determine connectivity in an automated fashion is unique. Secondly, the simultaneous correction of patient motion and the determination of correspondence between the views is unique.

14. SUBJECT TERMS

breast cancer, digital mammography, 3-D breast imaging, computer-  
aided diagnosis, limited-view image reconstruction

15. NUMBER OF PAGES

35

16. PRICE CODE

17. SECURITY CLASSIFICATION  
OF REPORT

Unclassified

18. SECURITY CLASSIFICATION  
OF THIS PAGE

Unclassified

19. SECURITY CLASSIFICATION  
OF ABSTRACT

Unclassified

20. LIMITATION OF ABSTRACT

Unlimited

NSN 7540-01-280-5500

Standard Form 298 (Rev. 2-89)  
Prescribed by ANSI Std. Z39-18  
298-102

## FOREWORD

Opinions, interpretations, conclusions and recommendations are those of the author and are not necessarily endorsed by the U.S. Army.

N/A Where copyrighted material is quoted, permission has been obtained to use such material.

N/A Where material from documents designated for limited distribution is quoted, permission has been obtained to use the material.

N/A Citations of commercial organizations and trade names in this report do not constitute an official Department of Army endorsement or approval of the products or services of these organizations.

N/A In conducting research using animals, the investigator(s) adhered to the "Guide for the Care and Use of Laboratory Animals," prepared by the Committee on Care and use of Laboratory Animals of the Institute of Laboratory Resources, national Research Council (NIH Publication No. 86-23, Revised 1985).

X For the protection of human subjects, the investigator(s) adhered to policies of applicable Federal Law 45 CFR 46.

N/A In conducting research utilizing recombinant DNA technology, the investigator(s) adhered to current guidelines promulgated by the National Institutes of Health.

N/A In the conduct of research utilizing recombinant DNA, the investigator(s) adhered to the NIH Guidelines for Research Involving Recombinant DNA Molecules.

N/A In the conduct of research involving hazardous organisms, the investigator(s) adhered to the CDC-NIH Guide for Biosafety in Microbiological and Biomedical Laboratories.

  
PI - Signature 11/5/02  
Date

## Table of Contents

Cover.....	1
SF 298.....	2
Table of Contents.....	4
Introduction.....	5
Body.....	6
Key Research Accomplishments.....	32
Reportable Outcomes.....	33
Conclusions.....	34
References.....	35
Appendices.....	N/A



## 1 Introduction

An automated technique has been developed and evaluated to reconstruct 3-D binary images of breast calcifications. The reconstruction algorithm consists of segmentation, motion correction, correlation between views, 3-D binary limited-view reconstruction of each calcification, and 3-D rendering. Our previous work relied upon significant human intervention and judgment in producing the final 3-D image. In this grant, we sought methods to automate these tasks. Required were robust methods of identifying, segmenting and correlating (or pairing) calcifications between views.

The tasks of identifying and segmenting calcifications have been attempted on numerous occasions. These previous attempts have been used almost exclusively in computer aided diagnosis (CAD) systems. In such systems, the desire is to capture a sufficient number of calcifications to identify clusters of suspicious calcifications for evaluation by a human observer. Significant effort is expended on eliminating false positives. By imaging the breast at 3 separate angles with known spatial alignment, we have the advantage that true calcifications are present in each of the images, while most spurious or non-calcified signals are only found in one image. This additional constraint allows us to segment more calcifications in each image, admittedly with a higher false positive rate. The task of correlation between the images quite naturally reduces the false positive rate in the 3-D image.

The work of this grant is reviewed in this final report.

## 2 Body

### 2.1 Summary of Work Items

It is useful to restate the work items listed in the original grant. They are as follows:

- Task 1: Compile database of 50 selected cases (Months 1-2)
- Task 2: Manually identify and pair calcifications in database images (Months 3-4)
- Task 3: Evaluate methods for automated identifications, segmentation and correlation of calcifications (Months 1-24).
- Task 4: Apply reconstruction technique to non-calcified structures (Months 25-36)

### 2.2 Segmentation

#### 2.2.1 Image Processing

This section describes our algorithm for simultaneously identifying and segmenting calcifications in individual images.

Each image is represented as a  $1024 \times 1024$  array of 12-bit data, which represents a 5 cm by 5 cm region in an x-ray projection. Figure 1 shows an example of such an image. While the calcifications, which can be seen in the upper left hand corner, are darker than their immediate surround, the difference is not so large as the variation across the image due to the structures in the breast of much larger scale.

To remove these larger features and thereby reduce the dynamic range, a median filtered image is subtracted from the original image. That is, from each image pixel value is subtracted the median of a  $31 \times 31$  region containing the pixel. Figure 2 shows the image after subtraction of the median filtered image and after denoising the image. The denoising consists of replacing pixel values which differ by more than three (3) standard deviations from the mean, calculated for the surrounding  $5 \times 5$  region. The removed values are replaced with the average of the neighboring pixels.

To further emphasize the high frequency components of the image, a Laplacian operator is applied to the image. At each pixel, a quadratic fit is made to a  $7 \times 7$  neighborhood, and the coefficients of the un-mixed quadratic terms are used to estimate the Laplacian. The result of this operation is shown in Figure 3.



Figure 1: Sample digital image for identification and segmentation of calcifications.

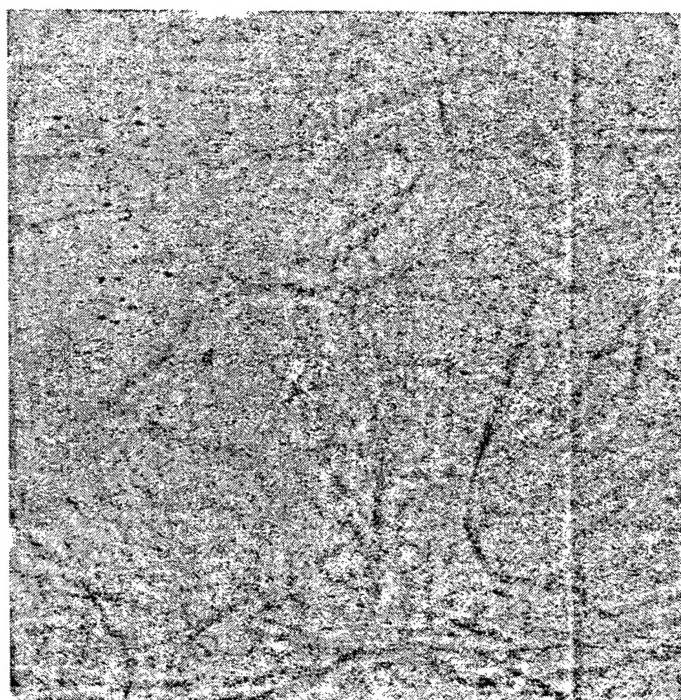


Figure 2: Digital image after subtracting the a median filtered image and removing high-noise pixels.

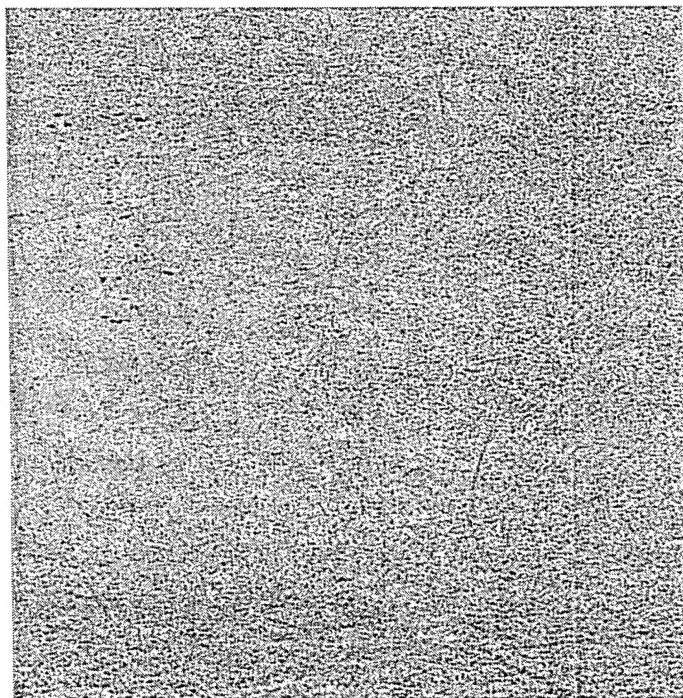


Figure 3: Digital image after applying (negative) Laplacian operator.

### 2.2.2 Segmentation of Candidate Calcifications

Figure 4 shows the Euler characteristic for the Laplacian image as a function of threshold. The intention is that this gives one a reasonable estimate of the threshold at which to segment the Laplacian image. A discussion of the Euler characteristic and several tests on simulated data is given in section 2.4.

Figure 5 shows a segmentation obtained by including all pixels in the Laplacian image (Figure 3) whose values are less than the threshold at which the Euler characteristic achieves one quarter of its maximum value. The cluster of calcifications in the upper left hand corner is clearly visible. While a significant number of other pixels are also identified, even in the segmented image most of these appear as a "dust" which a human observer would understand is not to be considered calcified material. The intention of the remainder of the algorithm is to computationally reject these false positives, based upon the segmentation and information in the original image. First, however, note that the segmentation is stable in the sense that, if instead of choosing the point at which the Euler characteristic achieves 25% of its maximum, one chooses 50%, the resulting image is quite similar, as can be seen in Figure 6. In order to guard against any significant variation in the statistics of an image across the image (for example, in some of our images part of the detector is directly exposed to the x-ray beam)

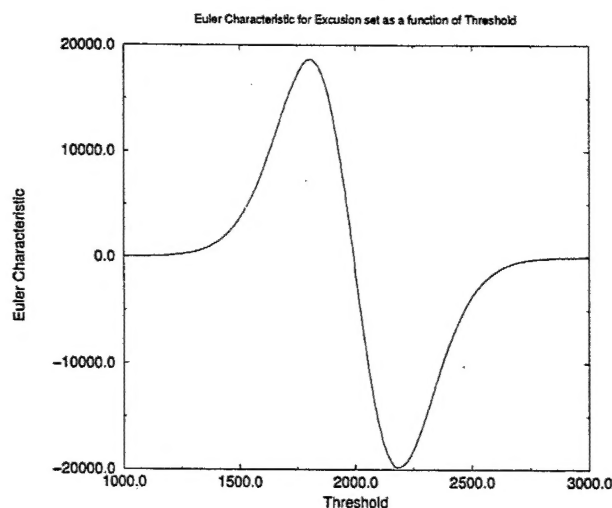


Figure 4: Euler characteristic of Laplacian image as a function of threshold.

the image is divided into overlapping  $250 \times 250$  pixel regions and the collection of all pixels so selected is used for the segmentation (the overlap corresponds to advancing the  $250 \times 250$  in steps of one third the size of the window).

Calcification candidates are then constructed as collections of contiguous pixels, using four-way continuity. For the x-ray image from which images 1–6 have been derived, the algorithm (using a threshold of 25% of that at which the Euler characteristic obtains its maximum) gives 1677 candidates.

### 2.2.3 Feature Analysis

For each calcification candidate, a variety of features are calculated. The first set of features uses a rectangular region from the denoised image containing the pixels in the calcification candidate and extending a further 7 pixels in each direction. Within this region, all pixels that would be segmented by a cut-off corresponding to 35% of the Euler characteristic maximum (this excludes slightly more than the pixels in the actual calcification candidates) are used for a quadratic fit which serves as an estimate of the background of the calcification. Thus, the pixels are identified by the using the heuristic involving the Laplacian image and the Euler characteristic as a function of threshold, but the region being used here is the corresponding region in the de-trended and de-noised image, *e.g.* Figure 2. From this fit the following features are estimated:

*max depth* The maximum difference between the fitted quadratic background and the actual image value at any pixel associated with the calcification candidate.

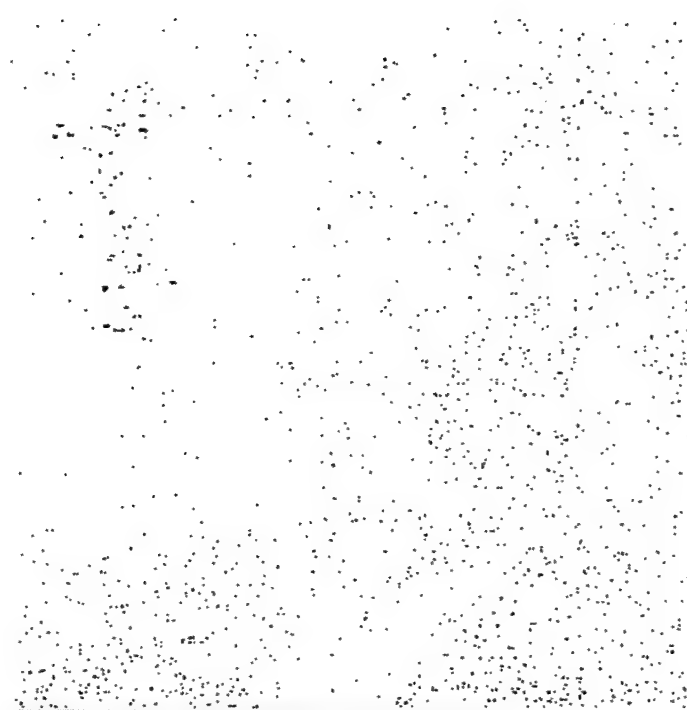


Figure 5: Segmentation based on Laplacian image at the point where the Euler characteristic reaches 25% of its maximum.



Figure 6: Segmentation based on Laplacian image at the point where the Euler characteristic reaches 50% of its maximum.



*ave depth* The average difference between the fitted quadratic background and the actual pixel values.

$\chi_f^2$  The value of  $\chi^2$  per degree of freedom, as a measure of how well the quadratic fit the background.

$\chi_{calc}^2$  The sum of the squares of the differences between the values of the pixels in the candidate and the estimates of those values from the fit to the background.

The distributions of maximum and average depth features are shown in figure 7. The distributions of  $\sqrt{\chi_f^2}$  and  $\chi_{calc}^2$  are shown in figure 8.

Another set of features are calculated in an attempt to exclude false calcification candidates which are associated with linear anatomical features. Figure 9 shows a linear feature in which three presumably incorrect candidates have been identified. In this image, the linear feature is roughly in line with the long axes of the calcifications. For each calcification candidate, the pair of pixels that are separated by the greatest Euclidean distance is identified, and the line through this pair is considered to be the long axis of the calcification. The width of the calcification is then identified as twice the farthest distance of any candidate pixel from the long axis. A region 7 times the length of the calcification and 8 times the width is then divided into three regions parallel to the long axis of the calcification, and the average of each region is used as a statistic. The resulting statistics of this procedure are

*aspect ratio* The ratio of the width of the candidate to the length.

$\mu_{online}, \sigma_{online},$

$\mu_{+side}, \sigma_{+side},$

$\mu_{-side}, \sigma_{-side}$  For these quantities, three rectangular regions whose long axes are parallel to the long axis of the candidate are used. The "on line" region contains the calcification, while the other regions lie to either side (the sign is an arbitrary label). For each region, the average pixel value  $\mu$  and the standard deviation  $\sigma$  in the set of pixel-values is calculated.

The distributions of these values are shown for all candidates and selected candidates in Figures 10 and 11.

In an additional search for large scale structures which can produce false positives, an additional set of statistics are calculated as follows. First, the average and population variance of the pixels in the candidate calcification are determined. Second, the average and population variance of the pixels in an approximately  $300 \times 300$  pixel region around the calcification candidate are calculated. Finally, starting with the calcification, one determines the largest connected region such that all of the pixels in that region are less than the average over the  $300 \times 300$  region by one population variance. This new region is intended to represent any large scale structure in which the candidates are

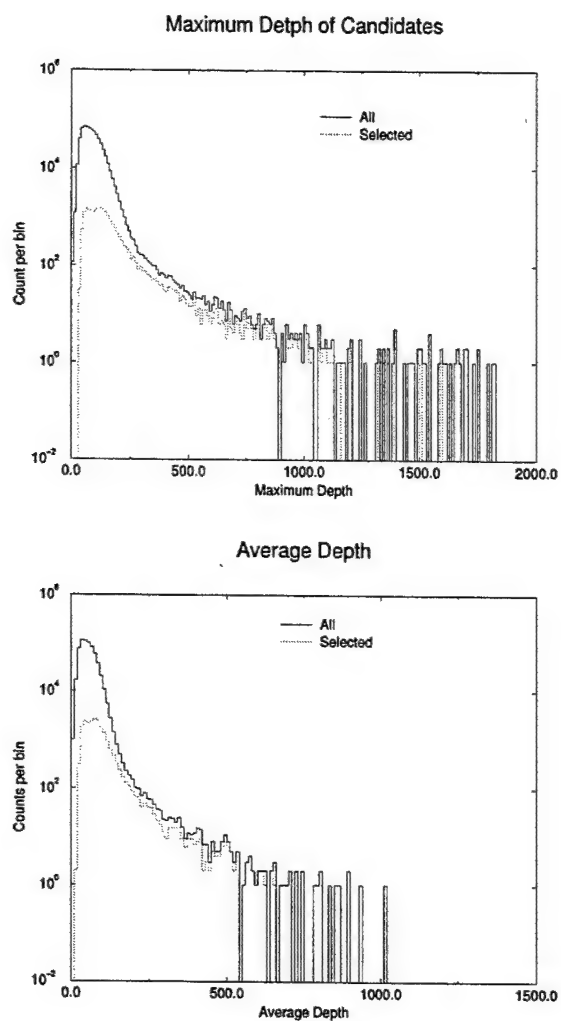


Figure 7: At top, the maximum depth feature for all calcification candidates and for the finally selected set. At bottom, the average depth feature.

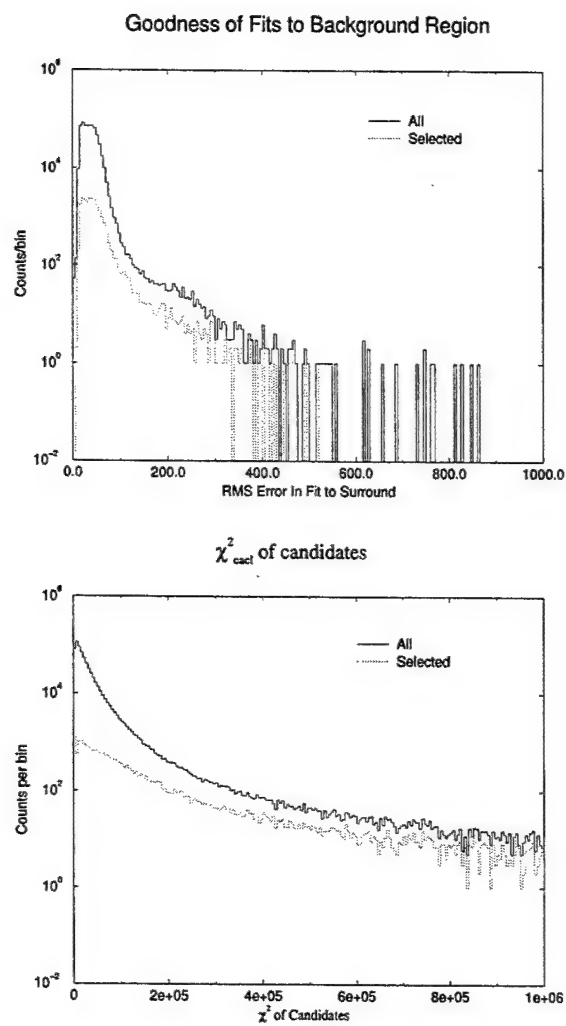


Figure 8: At top,  $\sqrt{\chi^2_f}$ , indicating the goodness-of-fit to the background in units of digital levels. At bottom,  $\chi^2_{\text{roi}}$ , measuring size and contrast of the candidate.

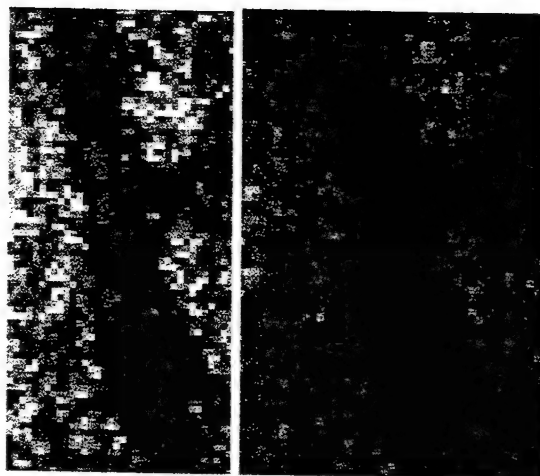


Figure 9: (Left) Linear detail with presumably false calcification candidates. (Right) Region identified as a possible larger structure in which these candidates are situated.

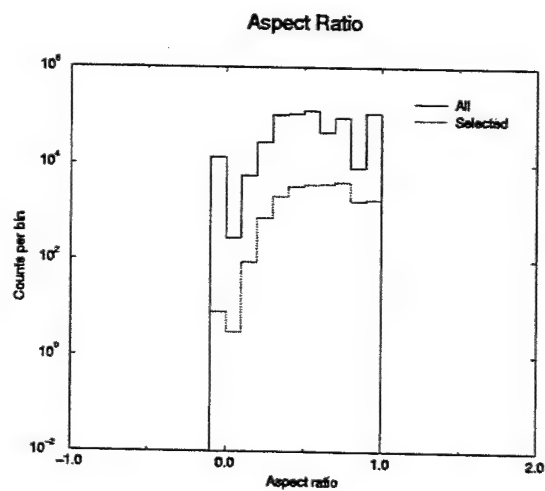


Figure 10: Aspect ratio of calcification candidates.

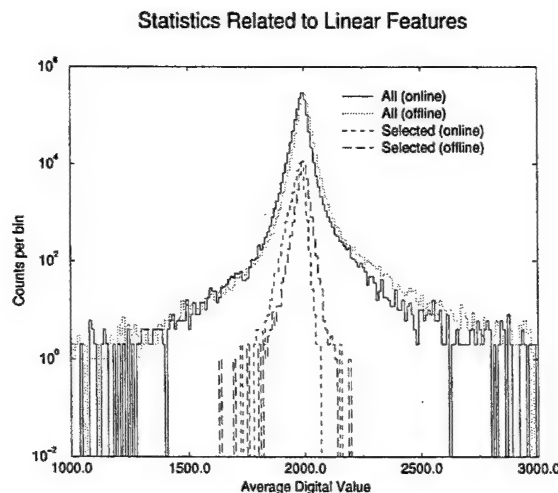


Figure 11: On-line ( $\mu_{\text{online}}$ ) and off-line ( $\mu_{+\text{side}}$  and  $\mu_{-\text{side}}$  combined). The on-line statistics have been scaled by a factor of 2.

located. Figure 9 shows an example of the region determined for the three candidates in one linear feature. Regions similarly associated with other calcification candidates are shown in Figure 12.

From this one obtains the following features:

- |  |   |
|--|---|
| $N_{\text{struct}}, \mu_{\text{struct}}, \sigma_{\text{struct}}$ | The number, mean, and population standard deviation of pixels identified as being in a possible large scale structure containing the calcification candidate. |
| $\mu_{\text{calc}}, \sigma_{\text{calc}}$                        | The mean and population variance of the pixels in the calcification candidate.  |
| $\mu_{\text{reg}}, \sigma_{\text{reg}}$                          | The mean and population variance of the pixels in the $300 \times 300$ region.  |

The distributions of  $N_{\text{struct}}, \mu_{\text{struct}}, \mu_{\text{calc}}, \mu_{\text{reg}}$  are shown in Figure 13.

To remove false positives, calcifications candidates are rejected for failing any of the following tests:

1. If the *aspect ratio*  $< 0.25$ , then candidate is assumed to be a linear anatomic feature and not a calcification.
2. If either of the side averages is significantly greater than the *on line average*, then the candidate seems to lie inside a linear feature and is rejected as a false positive. Specifically, if

$$\mu_{-\text{side}} - \mu_{\text{online}} > 5\sqrt{\sigma_{-\text{side}}^2 + \sigma_{\text{online}}^2}$$

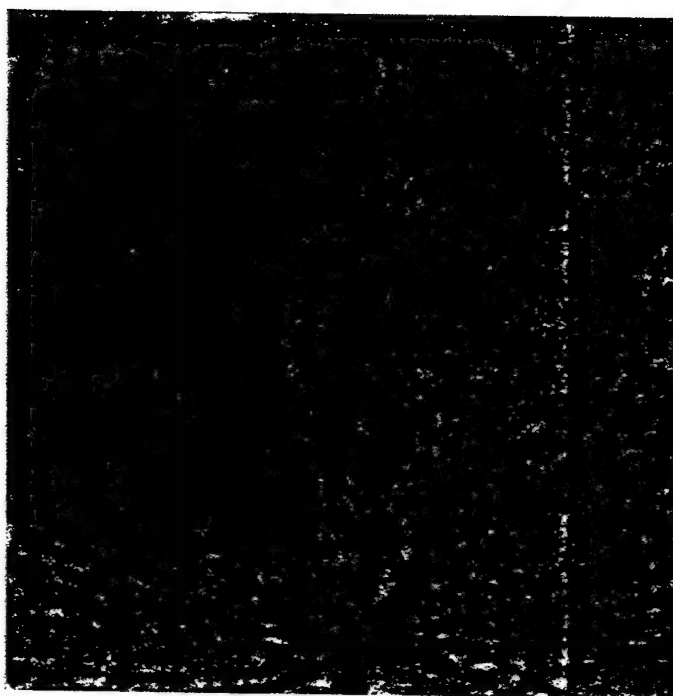


Figure 12: Segmentation of regions of large scale structure which might indicate that some calcification candidates are false positives.

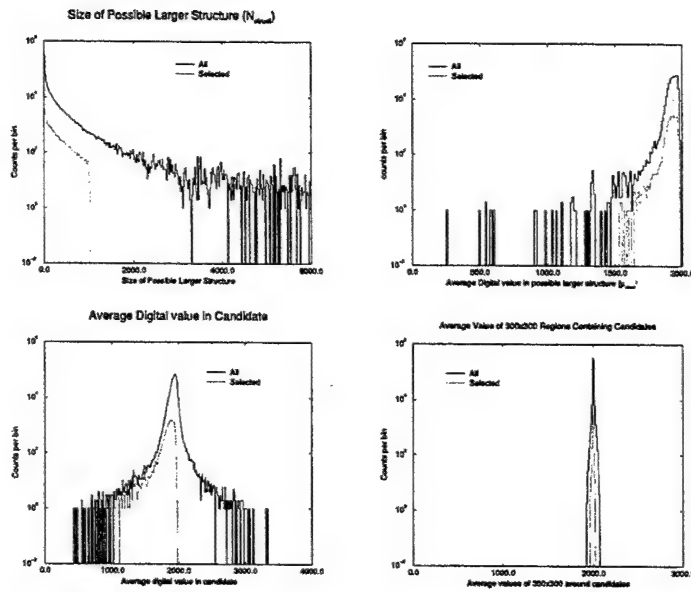


Figure 13: Values for the size of possible larger structures containing calcifications ( $N_{struct}$ ), the average value in such regions  $\mu_{struct}$ , the average digital value in calcification candidate  $\mu_{calc}$ , and the average value in  $300 \times 300$  pixel regions containing the candidates ( $\mu_{reg}$ ). These values are calculated from the image after unsharp masking, so the baseline value has been adjusted to 2000.

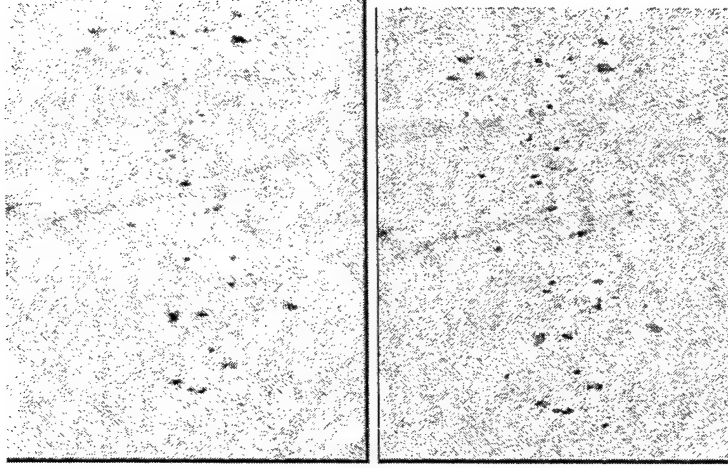


Figure 14: Example of a region in which calcification have been identified and segmented.

or

$$\mu_{+side} - \mu_{online} > 5\sqrt{\sigma_{+side}^2 + \sigma_{online}^2}$$

then the candidate is rejected.

3. If  $\chi_{calc}^2 < 25\chi_f^2$ , then the candidate is rejected. Note that for uncorrelated noise, this would correspond to a cutoff in the signal-to-noise ratio of 5.
4. If  $\mu_{reg} - \mu_{calc} < 2\sigma_{reg}$ , then the candidate is considered insufficiently dense to be a true calcification.
5. If  $max\ depth < 2\chi_f$  or  $max\ depth < 2\sigma_{reg}$ , the candidate is similarly rejected.
6. If  $N_{struct} > 1000$ , the candidate is assumed to be a false positive resulting from a large scale anatomical structure.
7. If  $N_{struct}$  is greater than twice the number of pixels in the candidate and  $\mu_{struct} - \mu_{calc} < \sigma_{struct} + \sigma_{calc}$  then the candidate is rejected.

Figure 14 show a region containing calcifications that have been segmented. Some examples of candidates which are probably false positives are shown in figure 15.

#### 2.2.4 Performance

Having no true "gold standard" available, we compared the set of calcifications identified by our algorithm with those identified by a human observer. The



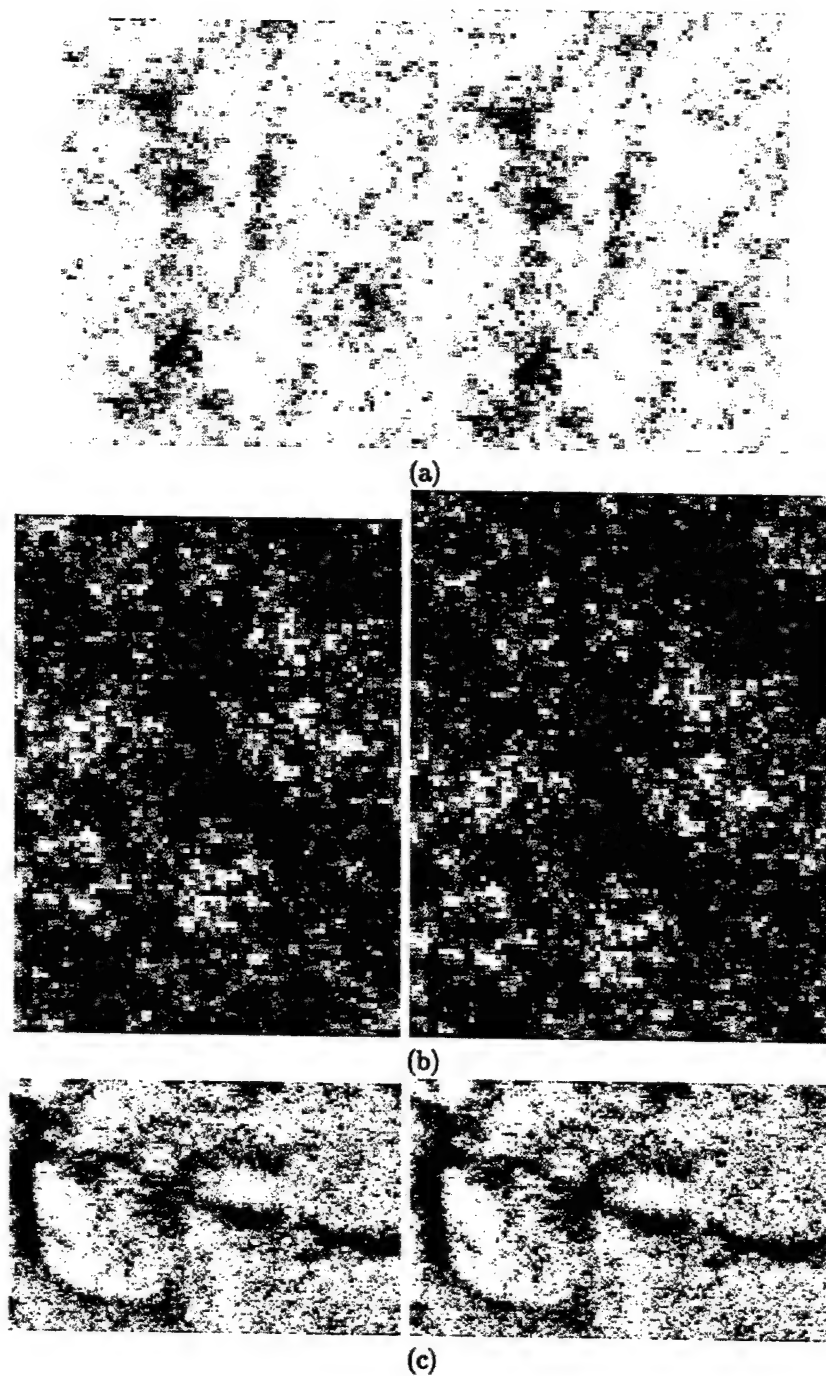


Figure 15: Example of probable false positives.

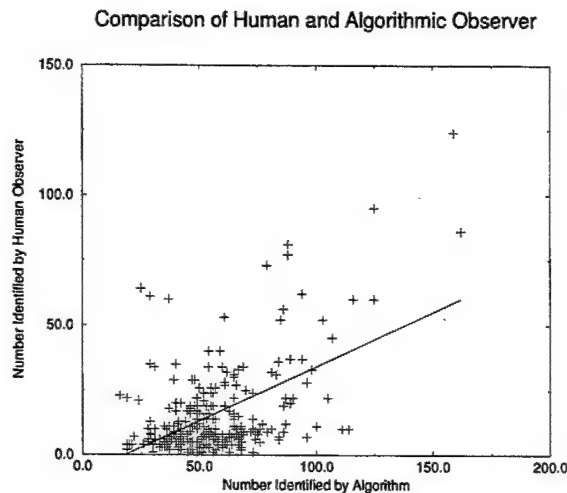


Figure 16: Comparison of the number of candidates detected by the algorithm with the number identified by a human observer.

human observer was a medical physicist familiar with mammography. A comparison of the number of calcifications detected in each image by the human observer with the number algorithmically detected is shown in figure 16, with a correlations coefficient of 0.5. Figure 17 shows the fraction of calcification detected by the human observer which were also detected algorithmically, and also the fraction of the calcifications detected algorithmically which were detected by the human observer. Approximately one half of the manually identified calcifications were identified algorithmically.

Retrospectively, among the calcifications identified algorithmically but not identified by the human observer, there was a continuum ranging from shadows which were almost certainly not calcifications, through various degrees of ambiguity, to objects which were almost certainly calcifications which had been overlooked by the human observer. A subset of the images had been similarly analyzed by a second human observer, also a physicist. Agreement between physicists was about as good as agreement between the algorithm and each physicist. We have discussed with radiologists the fact that there seems to be an irreducible degree of ambiguity in deciding which shadows on a mammogram represent calcifications and which ones don't. This makes it difficult to "tune" an algorithm in a meaningful manner.

### 2.3 Correlation

Each calcification lies on the geometric line from the position of the x-ray focus at the time of acquisition to the position of the shadow of the calcification in

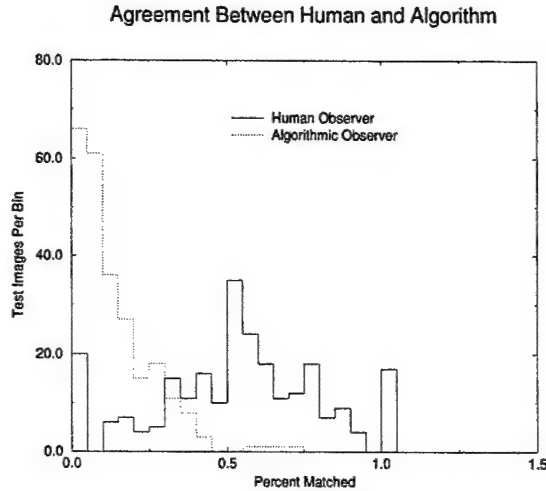


Figure 17: Fraction of candidates identified by the human or algorithmic observer upon which the two observers agree upon the presence of a calcification.

the image. Thus, for corresponding calcifications in multiple images, the lines-of-sight connecting the x-ray foci and the projections must intersect at the position of the calcification in space. This requirement allows one to identify shadows corresponding to the same projection in multiple images.

In practice, we have found several issues that confound this approach. One issue is that candidates visible in one image occasionally are not visible in the second image or overlap other calcifications, precluding a unique matching of calcifications. A second issue we have found is that projected shadows are often not consistent with any matching between images. This appears to be due to a combination of patient motion and some uncertainty or instability in the acquisition geometry.

As a result, both the matching problem and the geometry correction problem must be dealt with simultaneously. The most general possible geometric correction would introduce a large number of parameters to fit. We have settled on providing an effective position adjustment of the data, consisting of a translation of the second off-axis image in the horizontal direction and translations of the third (on-axis) image in both the horizontal and vertical directions. This combined algorithm is discussed in the next subsection.

### 2.3.1 Algorithm

For a point  $P$  and a line  $l$ , let  $d(P, l)$  be the perpendicular distance from the point to the line. For a given set of sight-lines  $l_1, l_2, l_3$ , each joining the position of the x-ray focus to the corresponding shadow of a calcification, the calcification

should lie at the common intersection. Due to experimental uncertainties, it is then reasonable to use as the position of the calcification the point which minimizes the distances to the sight-lines in a least squares sense, *i.e.*  $P_{\text{calc}}$  is the point  $P$  which minimizes:

$$d_{\text{rms}}(P, l_1, l_2, l_3) = \sqrt{(d^2(P, l_1) + d^2(P, l_2) + d^2(P, l_3)) / 3}. \quad (1)$$

The minimum RMS distance then gives an measures of how well the three sight-lines fit the hypothesis that they intersect at a point.

For a given adjustment of the acquisition geometry, it was necessary to examine all possible matches between shadows in each image. To remove matches that were clearly inconsistent, and thereby reduce the combinatorial complexity, the following preliminary test was performed. For each pair of projections in the off-axis images, the position of the hypothetical calcification corresponding to those two projections,  $P_{2\text{view}}$ , was determined by minimizing the RMS error using only the two view, *i.e.*:

$$d_{\text{rms}}(P, l_1, l_2) = \sqrt{(d^2(P, l_1) + d^2(P, l_2)) / 2}. \quad (2)$$

The point  $P_{2\text{view}}$  was then projected into the third view and only shadows within 0.72 cm of the projection of the hypothetical calcification were further considered. For all remaining triples, the values of  $d_{\text{rms}}$  using the three sight-lines was then computed.

All hypothetical matches of shadows between the three views were then sorted according to  $d_{\text{rms}}$ . Any set of three shadows in which one of the shadows had occurred in a set of three with a smaller  $d_{\text{rms}}$  was then removed from the list, so that each shadow belonged at most to one set of three shadows. As a measure of the overall success in fitting all of the calcifications, we calculated:

$$\text{GOF} = \sum_{(l_1, l_2, l_3)} \frac{1}{1 + d_{\text{rms}}^4(l_1, l_2, l_3) / d_{\text{cutoff}}^4} \quad (3)$$

where  $d_{\text{cutoff}} = 0.05\text{mm}$  and the sum runs over all matches of sight-lines which passed the preliminary discriminator as discussed in the previous paragraph and  $d_{\text{rms}} < d_{\text{cutoff}}$ .

The GOF (Goodness of Fit) score was then used to adjust the geometric acquisition parameters to approximately compensate for the uncontrolled geometric effects discussed above. The geometry was varied by shifting the second off-axis view up to 1 cm in the horizontal direction from its nominal position, and adjusting the third (on axis view) up to 1 cm in either the horizontal or vertical direction. Adjustments were made in steps of 48  $\mu\text{m}$ , corresponding to the size of the pixels. The adjustment which gave the best GOF was then taken as the best approximate compensation for the combination of patient movement and geometric uncertainty.

### 2.3.2 Results

Figure 18 shows three views acquired for one of our cases. Four of the calcification matches are shown by corresponding labels in the three images. The first

three matches (a, b, and c) are intuitively reasonable. The fourth match (d) is probably incorrect in the middle figure, due to the failure of the segmentation algorithm to locate the corresponding shadow in this region. Figure 19 shows the fraction of calcification candidates automatically identified in each image which were matched with candidates in the other two image. Figure 20 shows the distribution of  $d_{rms}$  for all calcifications in all images.

## 2.4 Euler Characteristic

This section represents some notes on the use of the Euler characteristic.

### 2.4.1 Euler Characteristic

For a selected set of picture elements, the Euler characteristic represents the number of contiguous regions into which that set of elements can be divided minus the number of holes in those objects. In particular, the Euler characteristic can be computed for the excursion set (the set of pixels passing a given thresholding condition) as a function of threshold. As the Euler characteristic can be calculated in terms of local data, the Euler characteristic of excursion sets as a function of threshold can be calculated in a single pass through the image, making this calculation appealing for computational reasons. For stringent thresholding conditions (so that the excursion set is small) there are generally few holes in the resulting excursion set, so the Euler characteristic approximates the number of objects that would be in the binary image after thresholding. We looked at this with the intent that by studying the Euler characteristic as a function of threshold, one could then choose a threshold which reveals meaningful objects in the resulting segmentation. This is based loosely on the fact that human observers, when attempting to set such a threshold manually, have some success by looking for a threshold at the point at which distinct objects seem to appear.

### 2.4.2 Calculation of the Euler Characteristic

The Euler characteristic is equal to the number of regions minus the number of holes. The advantage of the Euler characteristic is that it can be computed from local data as

$$\chi = \#Faces - \#Edges + \#Vertices. \quad (4)$$

Given a set of pixels  $S$  in a square grid, two methods suggest themselves for computing the Euler characteristic. For the first method,  $\chi_A(S)$ , one considers each pixel to represent a square region of the plane. If the pixel is in the set  $S$ , then that pixel is included among the set of Faces, its four edges are included among the set of Edges, and its four vertices are counted among the set of Vertices. As each edge is shared by two pixels (except at boundaries) and each vertex is shared by four pixels (except at boundaries) one must take care to not count edges or vertices multiple times. A second method,  $\chi_B(S)$ , results

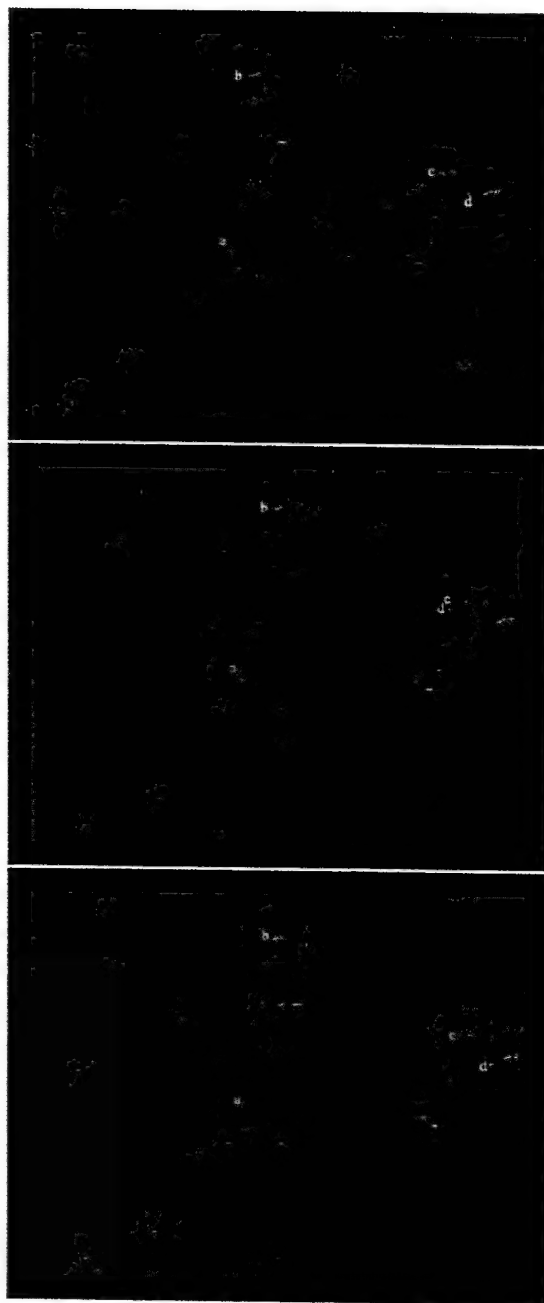


Figure 18: Segmentation in 3 views. Four three-way matches are shown, with root-mean-square distances to lines of (a) 0.002 cm, (b) 0.002 cm (c) 0.003 cm, and (d) 0.03 cm.

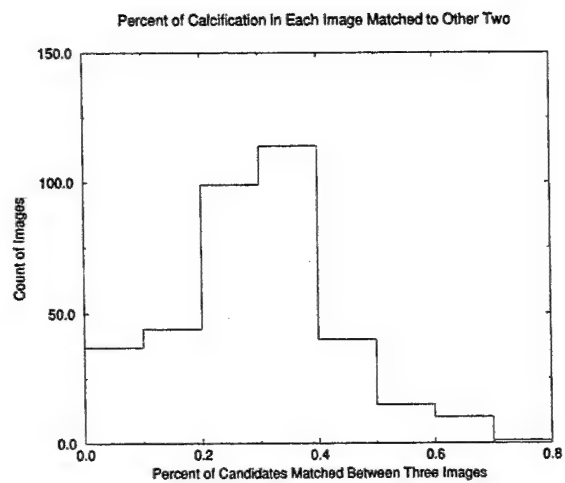


Figure 19: Percent of selected calcification candidates automatically matched.

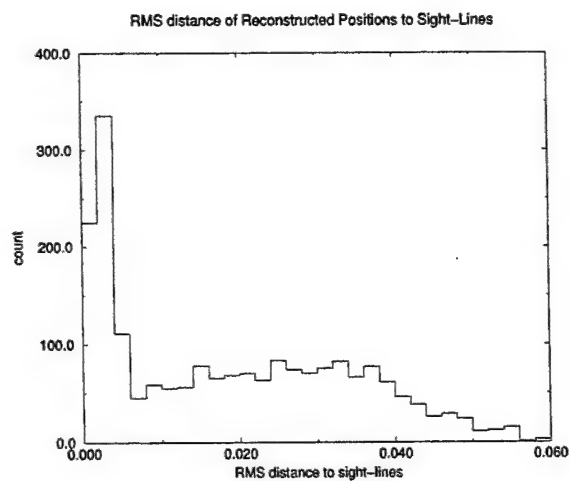


Figure 20: Root-mean-square distance to lines-of-sight from fitted positions calcifications

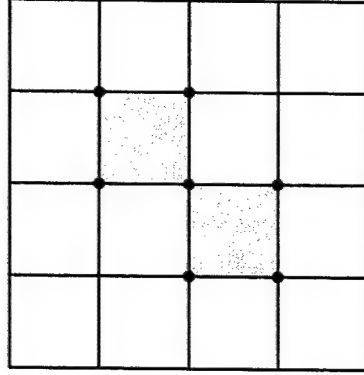


Figure 21: This set of pixels can count as one or two objects:  $\chi_A = 1$  and  $\chi_B = 2$ .

from considering each pixel value to be a sample point at the center of the pixel. The number of vertices is then given by the number of pixels in the set  $S$ , the number of edges is given by the set of horizontal or vertical edges between adjacent pixels in  $S$ , and the number of Faces is given by sets of four pixels with coordinates  $(i, j)$ ,  $(i, j + 1)$ ,  $(i + 1, j)$  and  $(i + 1, j + 1)$  all of which are in  $S$ .

The values of  $\chi_A$  and  $\chi_B$  are not identical, as seen in Figure 21. The set of pixels  $S$  in this image could be reasonably grouped into one or two objects. According to the counting rules for  $\chi_A$ , there are a total of two faces, eight edges, and seven vertices (noting not to double count the shared corner), giving  $\chi_A(S) = 1$ . According to the  $\chi_B$  rules, there are no faces or edges, but there are two vertices (corresponding to the sample points at the centers of the pixels) so that  $\chi_B(S) = 2$ .

The counting rules are dual in the sense that if the entire square grid is divided into two disjoint sets  $S$  and  $S'$ , then

$$\chi_A(S) + \chi_B(S') \approx 0, \quad (5)$$

*i.e.* every object in  $S$  is a hole in  $S'$  and vice-versa. The equality can not be exact due to the presence of a boundary, as connected regions of one set which reach the boundary are not counted as holes in the other set. In order to remove the issue of boundary conditions, for the remainder of this paragraph we will assume periodic boundary conditions. The equality in equation 5 is exact under these boundary conditions, so that the approximation in equation 5 under the boundary actually implemented is simply related to ignoring boundary effects. Now to understand equation 5, observe that every pixel is either in  $S$  or  $S'$ . If it is in  $S$ , then it contributes a face according to the  $\chi_A$  counting rules, while if it is in  $S'$  then it contributes a vertex according to the  $\chi_B$  counting rules, so



that

$$\#Faces_A(S) + \#Vertices_B(S') = N \quad (6)$$

where  $N$  is the total number of pixels in the grid. Further, given two adjacent pixels (either horizontal or vertical) then, it is either the case that at least one of the pixels is in  $S$ , so that the common edge between the pixels contributes to the number of edges according to the  $\chi_A$  rules, or both pixels are in  $S'$ , in which case the edge between the sample points contributes to the number of edges according to the  $\chi_B$  rules, and as these cases are mutually exclusive one has

$$\#Edges_A(S) + \#Edges_B(S') = N_{edge} \quad (7)$$

where  $N_{edge}$  is the total number of edges. Similarly, every corner of every pixel is either the corner of a pixel in  $S$  or is the corner of four pixels with sample points in  $S'$ , and again as these cases are mutually exclusive one has

$$\#Vertices_A(S) + \#Faces_B(S') = N_{vertices} \quad (8)$$

where  $N_{vertices}$  is the number of corners of all pixels in the image. Combining equations 6, 7, and 8 and noting that, with periodic boundary conditions  $N - N_{edge} + N_{vertices} = 0$ , one obtains the result given by equation 5.

The ambiguity in choosing between the counting rules corresponding to  $\chi_A$  and  $\chi_B$  produces several odd features. Note, for example, that if the set of pixels shown in gray in Figure 21 are taken as the set of pixels of interest, then one object is visible, but if the two pixels are taken as the excluded set, then there are two holes in the region. This asymmetry produces some counter-intuitive results. For example, if the random process generating the field of pixels values produces values symmetrically relative to some mean value (as, for example, a Gaussian random field) then one would intuitively expect that the Euler characteristic for the excursion set as a function of threshold would be symmetric with respect to the mean value of the field. However, because of situations like the above, configurations like that in Figure 21 carry more weight as "holes" than as pixels that are part of the segmentation, so that the curve is not symmetric. Instead, the Euler characteristic tends to be negative at a threshold corresponding to the image mean and the magnitude of the most negative value is greater than the magnitude of the highest value.

It is interesting to note that the following change of rules removes this ambiguity. Consider the pixel values localized on "sample points", each sample point being a possible vertex in the selected set. As before, let edges be lines between adjacent vertices. However, choose the lines between adjacent vertices in such a way that the resulting set of vertices and line segments results in dividing the plane up into triangles (requiring, of course, that two distinct segments meet only at vertices corresponding to sample points and that no point is inside two distinct triangles). Now use the resulting triangles as candidates for faces, the triangle serving as a face if and only if all three vertices are in the set  $S$ . Under these rules, there are no ambiguities analogous to that in Figure 21, and one can prove that (again requiring periodic boundary conditions)

$$\chi(S) + \chi(S') = 0 \quad (9)$$

where the Euler characteristics for both sets are computed by the same rules, as described earlier in the paragraph.

### 2.4.3 Random Field Examples

Figure 22 shows each component of the Euler characteristic and the Euler characteristic itself (according to the  $\chi_A$  rules) as a function of threshold, normalized by the number of pixels in the image. The simulation in Figure 22 corresponds to white Gaussian noise on a  $2048 \times 2048$  grid. As is well known[1], the curves in Figure 22 can be calculated from a simple theoretical argument. Given that

$$P(x \leq t) = \frac{1}{2} \left( 1 + \operatorname{erf} \left( \frac{x}{\sqrt{2}} \right) \right) \quad (10)$$

is the probability of a given pixel having value  $x$  less than or equal to a threshold  $t$ , one can treat the inclusion of each possible face, edge, or vertex as a independent random event and obtain

$$\text{Faces}(t)/N = P(x \leq t) \quad (11)$$

$$\text{Edges}(t)/N = 1 - (1 - P(x \leq t))^2 \quad (12)$$

$$\text{Vertices}(t)/N = 1 - (1 - P(x \leq t))^4 \quad (13)$$

where  $N$  is the number of pixels in the image. When so calculated, agreement was found to be better than 1%.

Figure 23 shows the Euler characteristic as a function of threshold for four different noise sources. In each case, the threshold has been rescaled so that the horizontal axis is in units of pixel-standard-deviations relative to the image mean. The Gaussian noise is the same as in figure 22. The negative exponential and “power-of-cosine” curves correspond to two cases of noise which decreases with frequency, though in the first case the noise power spectrum is not smooth at zero frequency and in the second case it is. The “CT” noise corresponds to noise which ramps up with frequency, somewhat like CT noise. In the “pow-cos” case the noise results in very strong correlations and a few large regions, so the vertical axis has been rescaled.

### 2.4.4 Discussion and Summary of Scientific Results

In this grant, we generated a manually segmented and paired dataset of 110 patients images, which we have used as a “gold standard” in the evaluation of computer algorithms for identifying, segmenting and correlating calcifications. We have been able to develop two separate computer algorithms, one for segmentation of the regions, the other for correlating calcifications between the images. Both are quite robust. There are a number of significant findings from this work that will be published. First, the use of the Euler characteristic to determine connectivity in an automated fashion is unique. Secondly, the simultaneous correction of patient motion and the determination of correspondence between the views is unique.

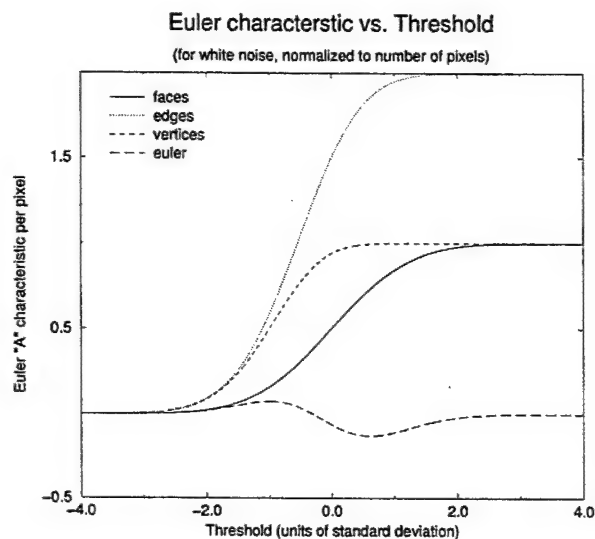


Figure 22:  $\chi_A$  and components as a function of threshold for white noise. Values have been divided by the number of pixels in the region. The horizontal axis is in units of standard deviations of the pixel values.

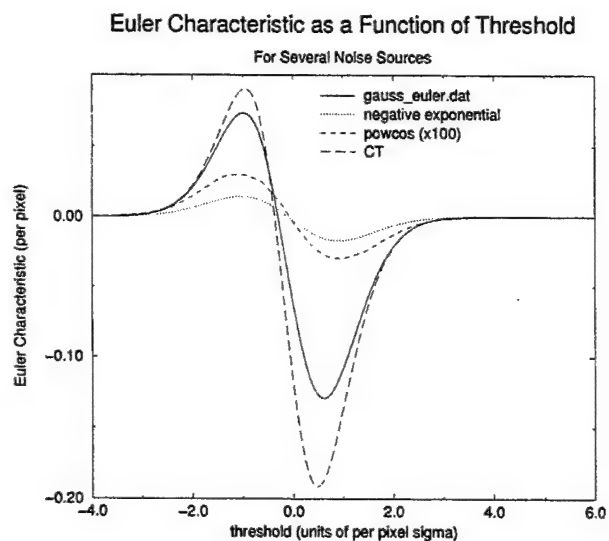


Figure 23: Comparison of  $\chi_A$  as a function of threshold for four different noise sources.

### 3 Key Research Accomplishments

The following is a list of key research accomplishments resulting from this work:

1. Developed a database of 110 biopsy-proven cases, with 3 digital images of each case
2. Developed a set of segmented images from each of 110 cases. In these data, each calcification from all three views of each patient was manually identified, and semi-automatically segmented.
3. Developed a set of manually determined correspondences.
4. These datasets were used to develop an automatic identification and segmentation algorithm that tested each point in an image as a potential seed point and then tested each resultant segmented region for validity as a potential calcification. A key feature of this algorithm was the use of the Euler characteristic to determine connectivity.
5. The above datasets were also used to develop an automatic correspondence algorithm. The algorithm used a weighted summation that allowed us to simultaneously correct for patient motion and determine optimal correspondence.

## 4 Reportable Outcomes

### 4.1 Published Manuscripts

1. A.D.A. Maidment, M. Albert, and E.P. Conant. Three-Dimensional Imaging of Breast Calcifications. In *Exploiting New Image Sources and Sensors*. Proceedings of the SPIE, 3240, 200-208 (1997).
2. A.D.A. Maidment, M. Albert, E.F. Conant, and S.A. Feig. Three-Dimensional Visualization of Breast Cancer. In *Digital Mammography '98*, edited by N. Karssemeijer, M. Thijssen, J. Hendricks, and L. van Erning, Kluvier, Holland, 57-60, (1998).
3. A.D.A. Maidment, M. Albert. Automated Reconstruction of 3-D Calcifications. In *IWDM 2000 5th International Workshop on Digital Mammography*, edited by M.J. Yaffe, Medical Physics Publishing, Madison WI, 72-80 (2001).

### 4.2 Abstracts and Presentations

1. A.D.A. Maidment, M. Albert, E.F. Conant, and C.W. Piccoli. A method for three-dimensional imaging of breast calcifications. World Congress on Medical Physics and Biomedical Engineering, Nice, France, Sept. 18, 1997. (Poster)
2. A.D.A. Maidment, M. Albert, E.F. Conant, and C.W. Piccoli. A method for three-dimensional imaging of breast calcifications. *Medical and Biological Engineering and Computing*, 35, Supplement Part 2, 751 (1997).
3. A.D.A. Maidment, M. Albert, E.F. Conant, S.A. Feig, C.W. Piccoli, S.A. Nussbaum, et al. A computer workstation for 3-D imaging of the breast. 83rd Scientific Assembly of the Radiological Society of North America, Chicago, IL, Nov. 30 - Dec. 5, 1997. (InfoRAD)
4. A.D.A. Maidment, M. Albert, E.F. Conant, S.A. Feig, C.W. Piccoli, S.A. Nussbaum, et al. A computer workstation for 3-D imaging of the breast. *Radiology*, 205(P), 741 (1997).
5. A.D.A. Maidment, M. Albert, and E.P. Conant. Three-Dimensional Imaging of Breast Calcifications. The 26th AIPR Workshop: Exploiting New Image Sources and Sensors, Cosmos Club, Washington DC, Oct. 16, 1997.
6. A.D.A. Maidment, M. Albert, E.F. Conant, and S.A. Feig. Three-Dimensional Visualization of Breast Cancer. 4th International Workshop on Digital Mammography, Nijmegen, The Netherlands, June 10, 1998.
7. A.D.A. Maidment, 3-D Imaging of the Breast. 6th International Cambridge Conference on Breast Cancer Screening. Cambridge, England. April 14, 1999.

8. A.D.A. Maidment, and M. Albert. "Automated Reconstruction of 3-D Calcifications". 5th International Workshop on Digital Mammography, Toronto, Canada, June 14, 2000.
9. A.D.A. Maidment. "3-D Imaging of the female breast". Imaging 2000, Stockholm, Sweden, June 29, 2000. (Invited Presentation)
10. A.D.A. Maidment, and M. Albert. "Automated 3-D Limited-View Binary Reconstruction of Breast Calcifications". 42nd Annual Meeting of the American Association of Physicists in Medicine, Chicago, IL, July 25, 2000.
11. A.D.A. Maidment, and M. Albert. "A Clinical Study of Calcifications Imaged by 2-D and 3-D Digital Mammography". DOD Era of Hope, Atlanta, GA, June 8- 11, 2000.
12. A.D.A. Maidment, and M. Albert. "3-D Digital Mammography: An Automated Method of Image Reconstruction". DOD Era of Hope, Atlanta, GA, June 8-11, 2000. A.D.A. Maidment, P. Bakic and M. Albert. "3-D Digital Mammography: A Comparison of Image Reconstruction Methods". DOD Era of Hope, Atlanta, GA, June 8-11, 2000.

### 4.3 Funding Applications

1. Andrew D. A. Maidment, Principle Investigator, DOD Breast Cancer Research Grant, DAMD17-98-1-8159, "3-Dimensional Imaging of the Breast". 7/98-6/2001.
2. Andrew D. A. Maidment, Principle Investigator DOD Breast Cancer Research Grant, DAMD17-00-1-0465, "A novel method for determining calcification composition", 7/00-6/03.

## 5 Conclusions

In conclusion, we have developed automated algorithms for identifying, segmenting, and correlating calcifications in 3-D, using 3 source images acquired at 15 degree increments. The algorithms have been tested with previously acquired clinical data, which was arranged into a database, and was analyzed by human observers for the purpose of developing a gold standard for the reconstructions. The algorithms have worked very well. The use of the Euler characteristic for connectivity analysis and the simultaneous correction of image correlation and image motion are particularly noteworthy accomplishments.

## 6 References

- [1] Klaus Voss. *Advances in Digital and Computational Geometry*, chapter Chapter 3: Discrete Integral Geometry and Stochastic Images, pages 87-111. Springer, Berlin, 1998.

## 7 Appendices

None

## 8 Research Personnel

Andrew D. A. Maidment, Ph.D.	Principle Investigator
Stephen Feig, M.D.	Radiologist
Catherine W. Piccoli, M.D.	Radiologist
Dionne Farria, M.D.	Radiologist
Michael Albert, Ph.D.	Programmer & Research Assistant.
Predrag Bakic, Ph.D.	Research Assistant.